metals

MDPI

Article

Study on Stress Corrosion Cracking Mechanism of Steel Wires with Different Strength Levels

Guangze Zhao, Xu Ma * and Ke Ma

School of Materials Science and Engineering, Tianjin University of Technology, Tianjian 300384, China
* Correspondence: maxumax@163.com

Abstract: In civil engineering, stress corrosion cracking (SCC) is a common cause of premature failure in steel wires, and effective solutions are currently limited. Investigating the SCC behavior of steel wires with different strength levels is crucial for understanding its fracture mechanism and developing potential solutions. This study examines the SCC behavior of wire rods with three strength grades (Steel A, B, and C) through stress corrosion experiments. The results show that high-strength wire rods have smaller pearlite interlamellar spacing. Steel C has the highest tensile strength (2303 MPa), while Steel A has the lowest (1830 MPa). Regarding stress corrosion sensitivity, the SCC mechanism of Steel C is dominated by hydrogen embrittlement, while Steels A and B primarily exhibit anodic dissolution as the cracking mechanism. Although Steel C has the smallest pearlite interlamellar spacing and superior corrosion resistance, its SCC failure time is the shortest due to hydrogen embrittlement. In contrast, for the anodic dissolution cracking mechanism, Steel B has a smaller pearlite interlamellar spacing, which enhances its corrosion resistance, and exhibits higher local stress stability due to its higher strength, resulting in the best SCC resistance (failure time: 3.81 h). This study reveals the synergistic effects of microstructure and strength on the SCC behavior of wire rods, offering theoretical guidance for the application of high-strength wire rods.

Keywords: wire rods; stress corrosion cracking; pearlite interlamellar spacing; hydrogen embrittlement; anodic dissolution

Academic Editor: Petros E. Tsakiridis

Received: 8 January 2025
Revised: 26 January 2025
Accepted: 27 January 2025
Published: 29 January 2025

Citation: Zhao, G.; Ma, X.; Ma, K. Study on Stress Corrosion Cracking Mechanism of Steel Wires with Different Strength Levels. *Metals* **2025**, *15*, 139. https://doi.org/10.3390/met15020139

1. Introduction

High-strength steel wires are extensively used in construction, bridges, and prestressed engineering due to their light weight, which reduces material usage and lowers manufacturing time and costs [1–3]. Given the increasing emphasis on energy efficiency and environmental protection, the high-strength design of steel wires has emerged as a key solution to meet the demands of modern engineering [4]. However, as the strength of the steel wires increases, their microstructure becomes more complex, which increases their susceptibility to stress corrosion in challenging environments [5–7]. High-strength steel wires are more vulnerable to stress corrosion cracking due to factors such as corrosion [8–11], hydrogen embrittlement [12–14], and external loads, which compromise their safety. As a result, stress corrosion failure has become a critical issue impacting the service life and safety performance of steel wires.

While considerable research has been conducted on the stress corrosion cracking (SCC) behavior of pearlitic steels, most studies focus on individual factors such as cold drawing, corrosive environments, or hydrogen embrittlement. There is a lack of systematic comparison and comprehensive analysis across different steel wires [15–17]. Jesús et al. [18] and Toribio et al. [19] studied the effect of cold drawing on the SCC behavior of pearlitic steels.

However, differences in experimental design and material composition led to significant discrepancies in their findings regarding SCC mechanisms. Torkkeli et al. [20] also examined the impact of pearlite microstructure on SCC mechanisms in fuel-grade ethanol (FGE) environments. They found that ferrite undergoes selective dissolution, while cementite becomes a more favorable cathode, leading to the formation of a microelectrochemical effect. This highlights the significant influence of the pearlitic microstructure on crack propagation and localized corrosion behavior in carbon steel under corrosive conditions. It also suggests that microstructural differences among various steel wires can result in distinct SCC mechanisms. Wang et al. [21] used a climate chamber to simulate corrosive environments and studied the effect of stress levels on corrosion damage. They found that high stress levels significantly accelerate the growth of microcracks, thereby reducing the ultimate strength of the steel wire. Therefore, maintaining consistency in experimental design is crucial when comparing different steel wires. While these studies highlight the significant role of a pearlitic microstructure in corrosive environments, systematic research on SCC behavior in steel wires with varying strength levels remains limited. Specifically, the relationship between microstructural features and SCC mechanisms has not been fully explored. Furthermore, due to variations in testing methods, processing techniques, and heat treatment conditions, comparing existing data remains challenging. Therefore, it is vital to examine the influence of the microstructure on SCC behavior and fracture mechanisms in steel wires of different strength grades, produced using the same processing technique.

This study investigates the microstructural evolution and fracture characteristics of three types of prestressed steel wires with varying strength grades in stress corrosion environments. This research aims to elucidate the mechanisms by which microstructure influences material properties and fracture behavior, providing scientific guidance for assessing stress corrosion resistance and fracture mechanisms of steel wires at various strength levels. This will offer a theoretical basis for material selection under different engineering conditions.

2. Materials and Methods

The experimental materials used in this study are different strength grades of wire steel SWRH82B produced by Tianjin NTS Flourish Co., Ltd., (Tianjin, China) with the chemical composition shown in Table 1. This material is widely used in the construction industry in China, and, due to its strength exceeding 1800 MPa, ultra-high-strength steel is more prone to stress corrosion cracking, making it of significant research importance. The cold drawing process involves the use of a 12 mm diameter experimental steel rod, which underwent nine drawing passes, ultimately resulting in a final diameter of 5.2 mm. The total strain, ε, is 1.6 ($\varepsilon = \ln(A_0/A)$, where A_0 is the initial cross-sectional area of the sample, and A is the cross-sectional area of the drawn sample, corresponding to a total reduction in an area of approximately 81.2%. Subsequently, the steel was annealed at 380 °C with a line speed of 100 m/min, ultimately producing a wire rod steel with a diameter of 5.2 mm, as shown in Figure 1b. Tensile tests were conducted using a WAW-2000G steel wire tensile testing machine (Jilin Testing Technology Co., Ltd., Jilin, China) with a gage length of 500 mm. The tensile rate before yielding is 0.15 mm/min, and the tensile rate after yielding is 2.5 mm/min, with three tests conducted.

Table 1. Chemical composition of experimental steels (wt.%).

	C	Mn	Si	P	S
A	0.84	0.74	0.25	0.0012	0.006
B	0.83	0.74	0.46	0.009	0.008
C	0.99	0.75	0.25	0.011	0.001

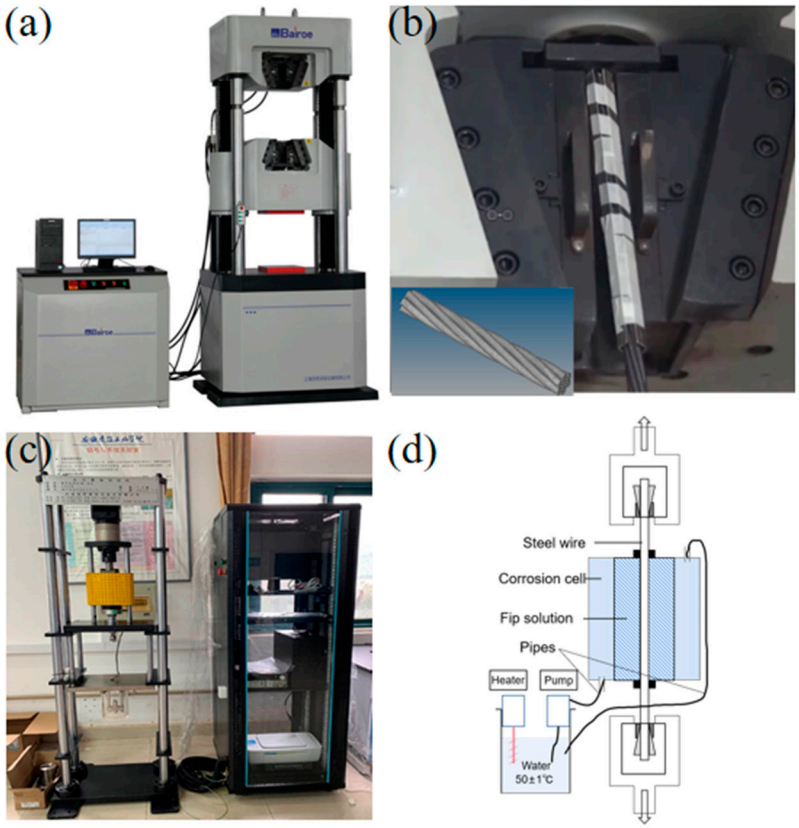

Figure 1. Schematic diagram of the tensile and stress corrosion experiments: (**a**) tensile testing machine; (**b**) schematic diagram of tensile test specimen; (**c**) stress corrosion testing machine; (**d**) and the schematic diagram of prestressed accelerated corrosion experimental device.

The experiment used wire cutting to obtain metallographic samples (5.2 mm × 10 mm) and transmission samples (3 mm × 0.4 mm) from different compositions of experimental steels along the longitudinal direction. After grinding and polishing with sandpaper, the samples were etched with a 4% nitric acid alcohol solution by volume. Subsequently, the microstructure of the cold-drawn experimental steel was observed using a field emission scanning electron microscope (Carl Zeiss AG, Oberkochen, Germany). For polished samples, electro-polishing is performed using a 10% perchloric acid alcohol solution at a temperature of −20 °C and a voltage of 20 V, with a polishing time of 60 s. The microstructure of the cold-drawn experimental steels with different compositions as analyzed using electron backscatter diffraction (Oxford Instruments, Abingdon, UK), and the raw data were analyzed using AztecCrystal (version 2.0) software. The transmission samples were ground to a thickness of 40 μm with sandpaper and then thinned using a double-spray thinning process in a 10% perchloric acid solution at 27 V and −25 °C. Subsequently, the microstructure of the experimental steel was further analyzed using a JEM-2100F field emission transmission electron microscope (JEOL Ltd., Beijing, China). This study used the latest residual stress measurement technique, Cosα method (Cr target XRD), to measure the residual stress values at the center of the surface of the stranded steel. During the experimental stage, the residual stress values were measured to observe the residual stress values of different strength grades of experimental steel after annealing. The principle of the Cosα method is to collect diffraction signals 360 ° in the same X-ray irradiation area to form a Debye ring. After each rotation of an angle $\alpha 1$, calculate the four types of strain on the grain at that angle, and substitute Equation (1) to obtain a constant a_1 value.

$$a_1 = \frac{1}{2}[(\varepsilon_{\alpha 1} - \varepsilon_{\pi+\alpha 1}) + (\varepsilon_{-\alpha 1} - \varepsilon_{\pi-\alpha 1})] \quad (1)$$

$\varepsilon_{\alpha 1}$, $\varepsilon_{\pi+\alpha 1}$, $\varepsilon_{-\alpha 1}$ and $\varepsilon_{\pi-\alpha 1}$ are the strain variables within the angle range of α1, and, so on, to obtain a_1~a_{90} (a_1 is a rotation of $\alpha_1 = 1°$, and a_{90} is a rotation of $\alpha_{90} = 90°$). a_1~a_{90} plot cosα1~cosα90, and, through linear regression, the slope of the line can be obtained. By incorporating the following Equation (2), the positive residual stress value σ can be obtained:

$$\sigma = \left[\frac{E}{1+V}\right] \frac{1}{\sin 2\eta} \frac{1}{\sin 2\psi} \left(\frac{\partial a}{\partial \cos \alpha}\right) \quad (2)$$

The stress corrosion cracking (SCC) sensitivity of wire rods with different strength grades was investigated by conducting experiments based on GB/T 21839-2019, "Test Methods for Steel for Prestressed Concrete" [22]. A 20% NH_4SCN solution was employed to accelerate the corrosion of the steel wire. The solution has a purity of at least 98.5%, with Cl^-, $SO_4{}^{2-}$, and S^{2-} concentrations below 0.005% and 0.001%, respectively. During the experiment, hydrogen gas was generated by ammonium decomposition, while thiocyanate ions prevented hydrogen gas formation from hydrogen ions, promoting the metal's hydrogen absorption. The stress corrosion cracking tests were conducted using an MTSWFW-50 stress corrosion testing machine (Jinan Metes Testing Technology Co., Ltd., Jinan, China), as shown in Figure 1c,d. The applied stress is 0.8 times the tensile strength. After fracturing, the sample's fracture surface was immediately cleaned with a distilled water and ethanol solution then blow-dried.

3. Results and Discussion

3.1. Microstructure and Mechanical Properties

Figure 2(a1–c1) present SEM images of the longitudinal sections of the experimental steels after cold drawing. The micrographs reveal that the pearlitic structure was aligned along the drawing direction (indicated by arrows in Figure 2) due to the severe plastic deformation induced by large strains during the cold drawing process. This deformation significantly disrupted the original lamellar pearlite structure, resulting in a highly fibrous microstructure. To further investigate the differences in the microstructure of the three experimental steels, EBSD analysis was conducted on the cold-drawn samples. The results showed that the grains in all experimental steels were elongated along the drawing direction, forming a pronounced fiber texture. These textures primarily consisted of four components: <110>, <112>, <113>, and <115>, with <110> being the most dominant. As shown in Figure 3, the <110> fiber texture component was most prominent in Steel C, reaching 67.1%. In comparison, Steel B exhibited a <110> component content of 59.6%, while Steel A had the lowest <110> component content at 58.1%.

To further investigate the microstructure after cold drawing, TEM was used to characterize the morphology of ferrite and cementite in the experimental steels, as shown in Figure 4. The results indicate that the steels retained their lamellar structure after annealing. Quantitative measurements of the pearlite lamellar spacing were conducted using Image-Pro (version 6.0) software, revealing that the pearlite lamellar spacings for Steels A, B, and C were 84.27 nm, 55.99 nm, and 38.28 nm, respectively.

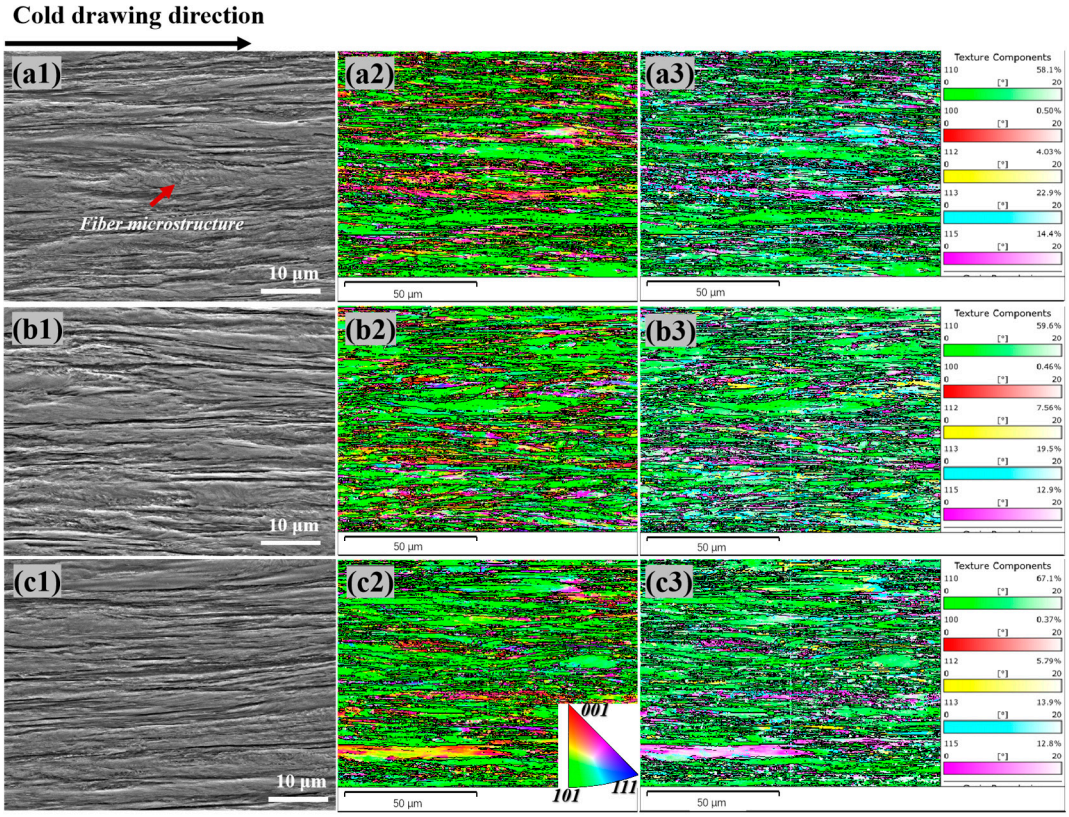

Figure 2. SEM images and EBSD orientation imaging maps of the experimental steels: (**a1**–**a3**) Steel A, (**b1**–**b3**) Steel B, (**c1**–**c3**) Steel C; red represents the <001> direction, green represents the <101> direction, and blue represents the <111> direction in the EBSD orientation image.

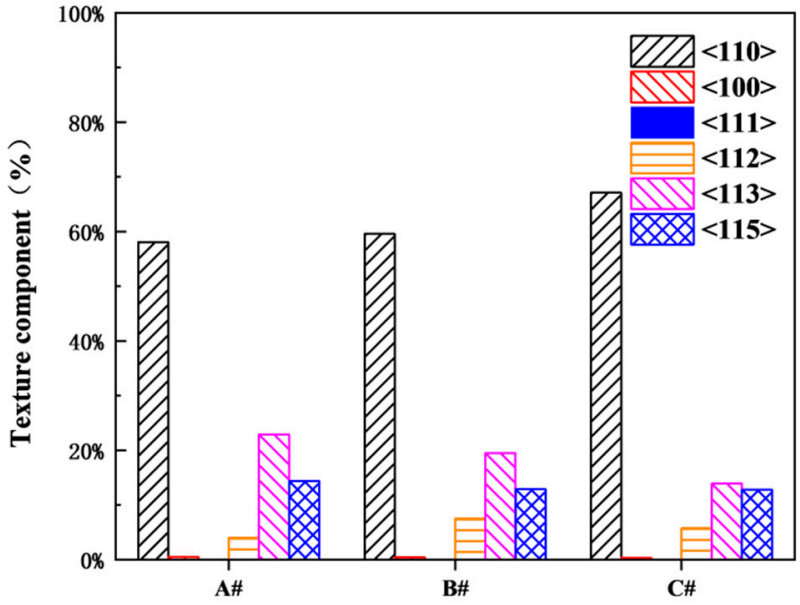

Figure 3. Proportions of texture components in experimental steels with different compositions.

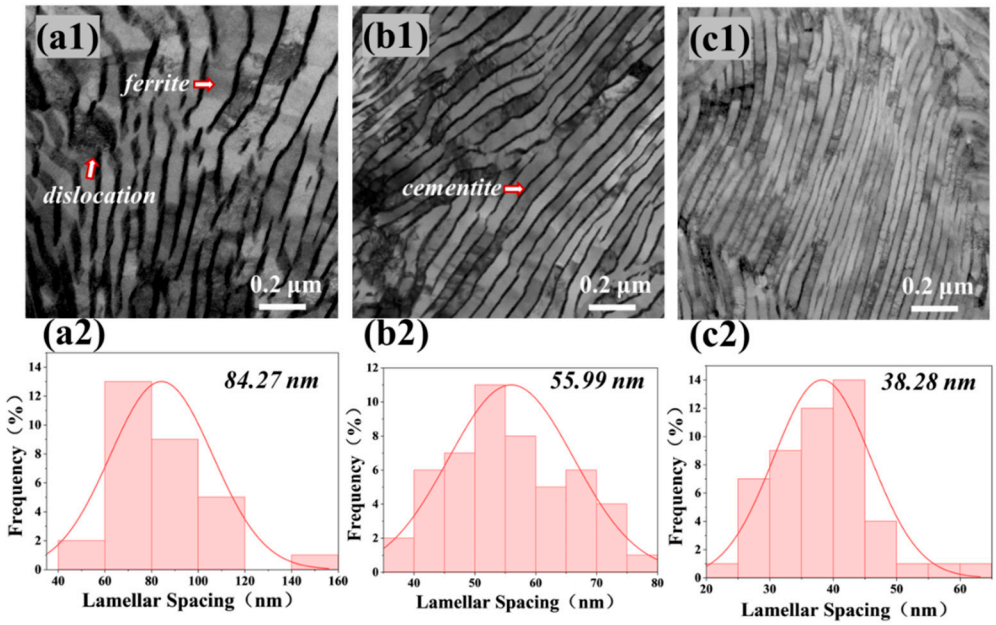

Figure 4. TEM images and statistical plots of lamellar spacing and cementite width for the experimental steels: (**a1**,**a2**) Steel A; (**b1**,**b2**) Steel B; and (**c1**,**c2**) Steel C.

Figure 5 shows the engineering stress–strain curves for the three experimental steels with different compositions, and the tensile performance results are summarized in Table 2. The tensile strengths of Steels A, B, and C were 1830 MPa, 2100 MPa, and 2303 MPa, respectively. All experimental steels demonstrated good elongation, with values exceeding 5%.

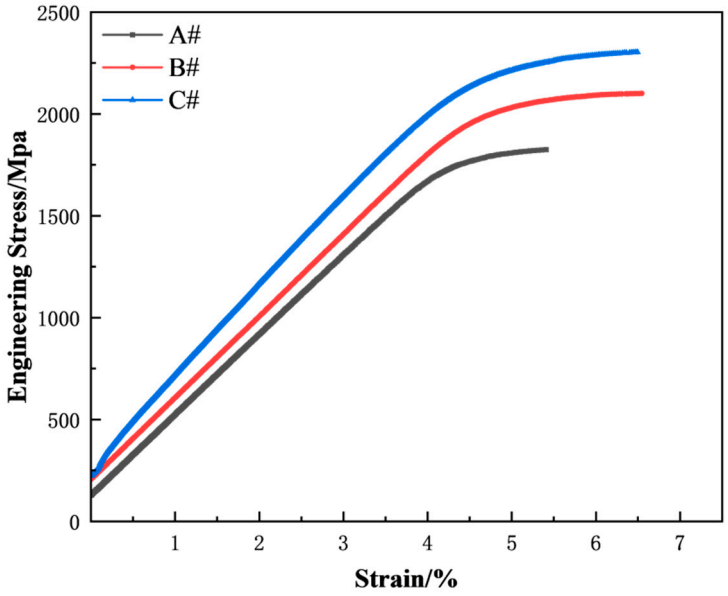

Figure 5. Engineering stress–strain curves of the experimental steels.

Table 2. Mechanical properties from tensile tests of the three experimental steels.

Steel Type	0.2% Yield Stress, σ0.2 (MPa)	Ultimate Tensile Stress, σmax (MPa)	Elongation, ε_m (%)
A#	1720	1830	5.2
B#	1779	2100	6.3
C#	2241	2303	6.2

The high strength of pearlite is mainly attributed to a combination of mechanisms, including interface strengthening, dislocation strengthening, and solid solution strengthening [23]. Zhang et al. [24,25] conducted a detailed study on the relationship between the microstructure and mechanical properties of cold-drawn pearlitic steel wire. They found that, as the drawing degree increased, both interface and dislocation strengthening effects were significantly enhanced. When the pre-drawing true strain reached 2.7, the dislocation density in the ferrite layers of the wire increased to approximately 8.8×10^{15} m^{-2}. The estimation results showed that interface and dislocation strengthening contributed 61% and 36% to the wire's strength, respectively, while the contribution from solid solution strengthening was negligible. Therefore, the strength differences observed in this experiment will be analyzed in terms of interface strengthening and dislocation strengthening. Figure 6 shows that the geometric dislocation densities of the experimental steels with different strength grades are 17.06×10^{14} m^{-2}, 17.12×10^{14} m^{-2}, and 16.92×10^{14} m^{-2}, respectively. This suggests that the dislocation strengthening effect contributes similarly to the strength differences among the three experimental steels. Figure 4 shows that the pearlite interlayer spacing of the three experimental steels varies as follows: Steel C < Steel B < Steel A, with the interlayer spacing of Steel A being twice that of Steel C. In pearlitic steel, the contribution of boundary strengthening is estimated by replacing the grain size with the interlamellar spacing of cementite. The Hall–Petch equation is as follows:

$$\sigma(b) = k(2d)^{-0.5} \quad (3)$$

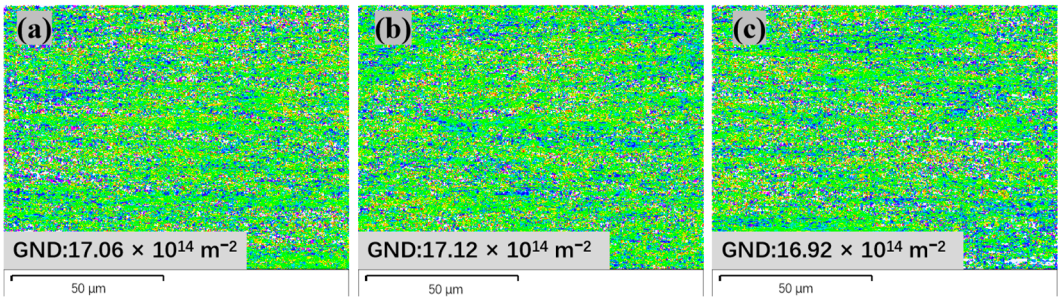

Figure 6. Geometric dislocation density image of stranded steel with different strength grades: (**a**) Steel A; (**b**) Steel B; and (**c**) Steel C.

According to the literature [24], k is a strain-dependent parameter, given by 0.41 $m^{-0.5}$. The boundary strengthening effects calculated for the three experimental steels are 1036 MPa, 1255 MPa, and 1510 MPa, respectively. This indicates that the strength differences between the experimental steels are primarily attributed to the influence of pearlite interlayer spacing.

3.2. Stress Corrosion Cracking Mechanism

Table 3 presents the fracture failure times of three different strength grade experimental steels in the stress corrosion experiment. The data indicate the following trend in stress corrosion sensitivity: Steel B < Steel A < Steel C. Among them, Steel B demonstrates the highest resistance to stress corrosion, with an average failure time of 3.81 h, while Steel C exhibits the poorest resistance, with an average failure time of 1.63 h. Notably, this result suggests that the resistance to stress corrosion is not directly related to the material's strength grade.

Table 3. Fracture failure times of experimental steels with different strength levels under stress corrosion.

Steel Type	A#	B#	C#
Failure time (h)	2.25	3.52	1.51
	2.29	3.73	1.55
	2.43	3.73	1.56
	2.55	3.88	1.61
	2.62	3.90	1.66
	2.63	3.92	1.68
	2.63	4.00	1.88
Average time (h)	2.49	3.81	1.63

The failure time is directly associated with the stress corrosion cracking (SCC) process [26]. The SCC process can be divided into three stages: the first stage involves crack initiation and nucleation, where localized effects of corrosion and tensile stress gradually lead to crack formation. The second stage is crack propagation, during which the cracks continuously grow. The third stage involves rapid crack growth, where localized stress concentration ultimately causes instantaneous fracture of the steel wire.

To investigate the stress corrosion cracking (SCC) mechanism of experimental steels with different strength grades, this study observed the characteristics of their tensile fractures and corrosion fractures in air (see Figure 7). The tensile fracture region exhibited significant plastic deformation, with Steels A and B showing mill-cutter-shear fractures, while Steel C exhibited a shear fracture. The cold drawing process led to grain deformation, an increase in dislocation density, and the strengthening of the <110> direction texture. These microstructural changes made the experimental steels more susceptible to additional shear stress in the transverse or vertical direction during tension. Since the steel wire undergoes plastic deformation during tensile testing, the shear stress generated along the 45° direction is the strongest, causing cracks to propagate in that direction and leading to fracture. Notably, Steel C has the highest <110> direction texture content, making it more prone to shear fractures.

In the stress corrosion cracking fractures, no significant plastic deformation features were observed. The surface was covered with reddish-brown corrosion products, accompanied by pitting on the wire surface. The stress corrosion fractures of Steels A and B were mill-cutter-shear fractures, with larger corrosion pits that were interconnected. In contrast, the stress corrosion fracture of Steel C was a shear fracture, with no corrosion products observed on the surface. The corrosion pits on the wire surface were distributed as small spots with greater depth. The stress corrosion fracture of Steel C showed a marked correlation with its tensile fracture mode, indicating that cracks in Steel C tend to propagate along the 45° direction under stress corrosion conditions. This trend may be related to the strengthening of its <110> direction texture, which makes the steel wire more prone to rapid crack propagation along this direction in a stress corrosion environment, resulting in shear fracture.

Further examination of the fracture morphology of the different strength grade experimental steels under stress corrosion cracking conditions reveals distinct features, as shown in Figure 8. Localized corrosion pits are visible on the fracture surfaces of Steel A and Steel B, showing typical signs of metal anodic dissolution and exhibiting characteristics of ductile fracture. Measurement of the pit depth from the surface of the sample reveals 0.22 mm for Steel A and 1.19 mm for Steel B, with the latter approximately five times deeper than the former. This suggests that Steel B has a certain resistance to the propagation of stress corrosion cracks. In contrast, the fracture surface of Steel C exhibits quasi-cleavage features accompanied by tearing, with no evidence of corrosive media. This indicates a typical

hydrogen embrittlement fracture, which is consistent with the hydrogen embrittlement fracture phenomena observed in many steel wires [18].

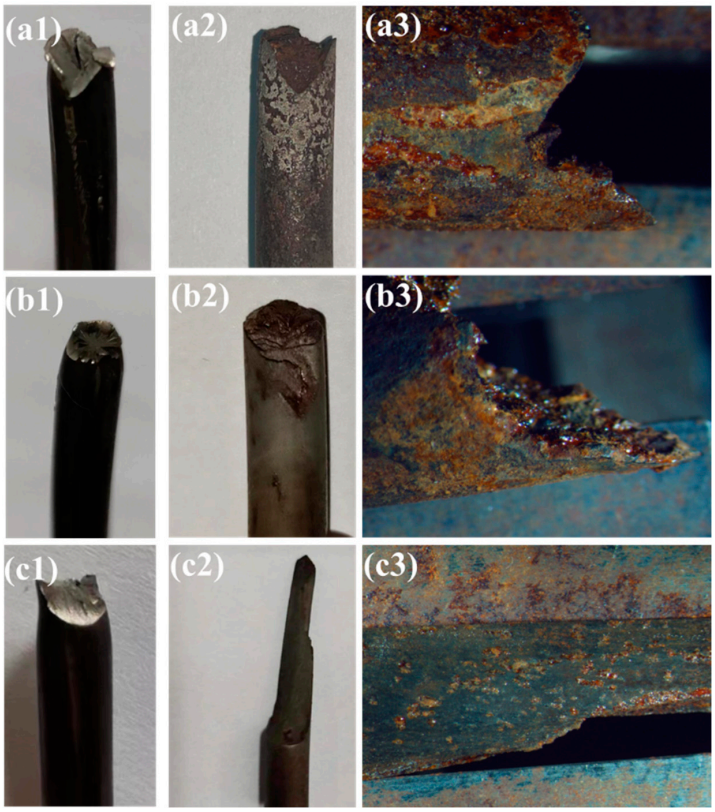

Figure 7. Tensile fracture surfaces and stress corrosion fracture surfaces of the experimental steels: (**a1**–**a3**) Steel A; (**b1**–**b3**) Steel B; and (**c1**–**c3**) Steel C.

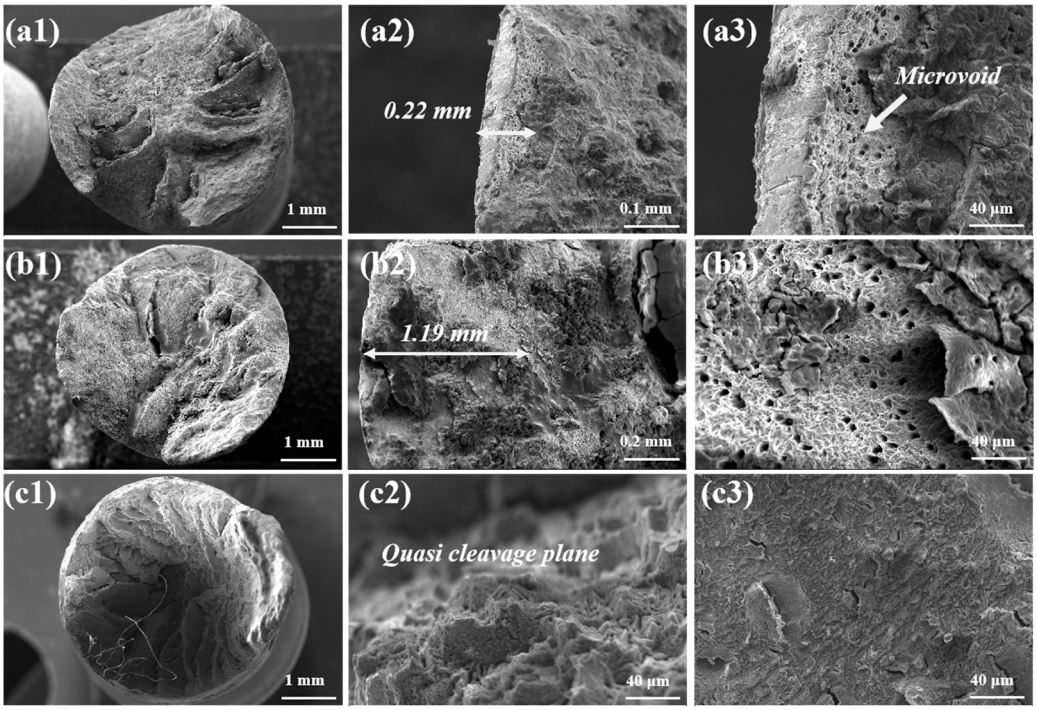

Figure 8. Stress corrosion cracking fracture surfaces of the experimental steels: (**a1**–**a3**) Steel A; (**b1**–**b3**) Steel B; and (**c1**–**c3**) Steel C.

The fracture morphology reveals that the stress corrosion cracking failure times of the different strength grade stranded steels are directly related to surface crack nucleation and corrosion mechanisms. To investigate this, surface residual stress analysis was performed on the three experimental steels, as shown in Figure 9. Steel A has the highest surface residual stress, at 48 MPa; Steel B follows with 24 MPa; and Steel C has the lowest, at 5 MPa. Research has shown that residual tensile stress causes surface stress concentration, which weakens the integrity of the passivation film [27]. Additionally, refining the pearlite interlamellar spacing can effectively reduce the corrosion rate [28]. Steel A, with the highest surface residual stress, severely damages the integrity of the passivation film. Its larger pearlite interlamellar spacing and the electrochemical potential difference at the ferrite–cementite interface exacerbate local corrosion reactions, leading to the rapid dissolution of ferrite and the formation of numerous corrosion pits on the surface. This results in the most severe corrosion and significantly shortens the crack nucleation time. In contrast, Steel B exhibits lower residual stress, which effectively reduces the risk of passivation film rupture. Its smaller pearlite interlamellar spacing significantly decreases electrochemical activity at potential crack initiation sites, thereby delaying corrosion pit formation and extending the crack nucleation time. Steel C, with the lowest surface residual stress and the smallest pearlite interlamellar spacing, demonstrates the best corrosion resistance. Consequently, it has fewer corrosion pits in the early stages of corrosion, which are smaller and deeper in nature. Overall, Steel C requires a longer time for crack nucleation during stress corrosion.

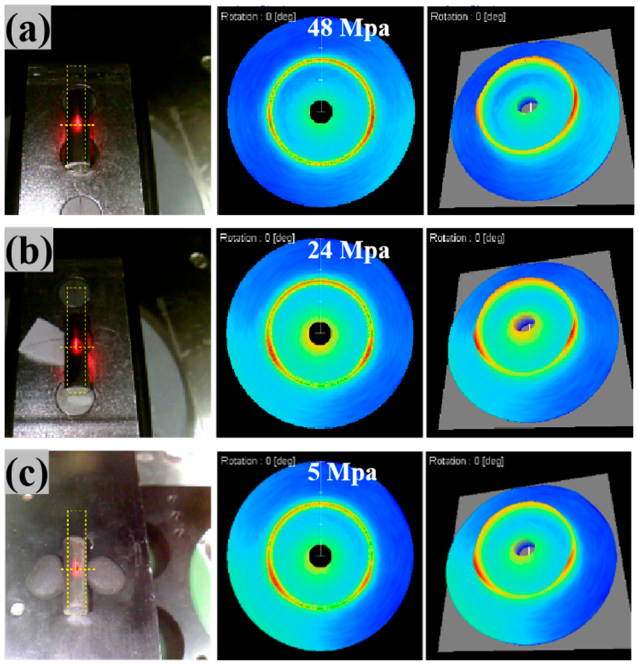

Figure 9. Byron ring on experimental steel surface: (**a**) Steel A; (**b**) Steel B; and (**c**) Steel C.

The three experimental steels show distinct fracture behaviors in stress corrosion cracking, which are closely linked to the surface pitting morphology. Steel A and Steel B form large, shallow pits in corrosive environments. During corrosion, the shallower pits promote the diffusion of hydrogen in the solution, resulting in a lower local hydrogen concentration. External anions migrate into the pits and react with metal ions, forming compounds that accumulate on the pit surface. These compounds hinder hydrogen diffusion into the metal, enhancing resistance to hydrogen embrittlement [29]. When cracks begin to form, the pearlitic lamellar structure, which aligns along the drawing direction after cold drawing, results in pits perpendicular to this direction. As the cracks propagate, they must gradually cross the pearlitic layers. Steel B not only has smaller pearlite interlamellar

spacing, enhancing its corrosion resistance, but its higher strength also improves local stress stability, resulting in the best resistance to stress corrosion cracking with a failure time of 3.81 h.

Zhang et al. [30] found that, in their study of the influence of currents on stress corrosion cracking mechanisms in bridge cable steel, hydrogen embrittlement results in a relatively flat surface on the steel cables. However, when anodic dissolution predominates, corrosion pits form on the steel cable surface. Another study also suggests that hydrogen embrittlement is caused by the formation of surface microcracks, where hydrogen accumulates at the crack tips, promoting crack propagation [31]. Steel C, with its smallest pearlite interlamellar spacing and higher surface residual stress, enhances corrosion resistance, leading to localized pitting. However, after microcrack formation, the smaller pearlite interlamellar spacing increases the ferrite–cementite interface area, accelerating hydrogen diffusion and significantly reducing the time to stress corrosion failure. Additionally, Steel C has the highest <110> texture content, resulting in the greatest phase anisotropy. Under applied stress and hydrogen, cracks are more likely to propagate along the texture direction, resulting in the formation of cleavage fracture surfaces.

4. Conclusions

This study systematically investigated the microstructure, mechanical properties, and stress corrosion cracking (SCC) behavior of prestressed steel wires with different strength levels. The main conclusions are as follows:

(1) Steel C has the highest tensile strength at 2303 MPa, followed by Steel B at 2100 MPa, and Steel A with the lowest tensile strength at 1830 MPa. The strength difference is primarily attributed to the boundary strengthening effect.
(2) The stress corrosion sensitivity follows the order: Steel B < Steel A < Steel C. The stress corrosion cracking mechanisms for the lower strength Steels A and B are anodic dissolution, while Steel C, with higher strength, exhibits hydrogen embrittlement.
(3) Although Steel C has the smallest pearlite interlamellar spacing and exhibits good corrosion resistance, its stress corrosion failure time is the shortest due to hydrogen embrittlement.
(4) Compared to Steel A, Steel B not only has smaller pearlite interlamellar spacing, enhancing its corrosion resistance, but its higher strength also improves local stress stability, resulting in the best resistance to stress corrosion cracking with a failure time of 3.81 h.

Author Contributions: Conceptualization, G.Z. and X.M.; methodology, K.M.; software, G.Z.; validation, X.M.; formal analysis, G.Z. and K.M.; data curation, G.Z. and X.M.; investigation, K.M.; writing—original draft preparation, G.Z.; writing—review and editing, X.M. and K.M.; visualization, G.Z. and K.M.; supervision, X.M. All authors have read and agreed to the published version of the manuscript.

Funding: This research received no external funding.

Data Availability Statement: The data presented in this study are available on request from the corresponding author. The data are not publicly available due to commercial confidentiality.

Acknowledgments: The authors are deeply grateful to Li Wang, Xuegang Zhao, and Lishan Hou from Tianjin NTS Flourish Co., Ltd. for providing experimental materials and assistance. Their invaluable opinions have significantly contributed to enhancing the manuscript.

Conflicts of Interest: The authors declare no conflicts of interest.

References

1. Li, H.; Yang, Y.; Wang, X.; Tang, H. Effects of the Position and Chloride-Induced Corrosion of Strand on Bonding Behavior between the Steel Strand and Concrete. *Structures* **2023**, *58*, 105500. [CrossRef]
2. Toribio, J.; Ovejero, E. Failure Analysis of Cold Drawn Prestressing Steel Wires Subjected to Stress Corrosion Cracking. *Eng. Fail. Anal.* **2005**, *12*, 654–661. [CrossRef]
3. Lee, J.; Lee, Y.-J.; Shim, C.-S. Probabilistic Prediction of Mechanical Characteristics of Corroded Strands. *Eng. Struct.* **2020**, *203*, 109882. [CrossRef]
4. Stovpchenko, G.; Medovar, L.; Stepanenko, D.; Jiang, Z.; Dong, Y.; Liu, Y. Energy and Environmental Savings by and for Steel Lightweight. *ISIJ Int.* **2024**, *64*, 165–173. [CrossRef]
5. Chen, M.; Lu, X.; Zhou, Z.; Du, Y.; Xu, X.; Li, X. Mechanical Properties of 2100 MPa Parallel Wire Strands under and after Elevated Temperature. *J. Constr. Steel Res.* **2024**, *212*, 108323. [CrossRef]
6. Liu, L.; Wang, L.; Yu, S.; Li, M. Mechanical Properties of Steel Strands Cooled by Different Methods After High-Temperature Treatment. *Int. J. Steel Struct.* **2022**, *22*, 333–342. [CrossRef]
7. Xie, J.; Zhao, X.; Yan, J.-B. Mechanical Properties of High Strength Steel Strand at Low Temperatures: Tests and Analysis. *Constr. Build. Mater.* **2018**, *189*, 1076–1092. [CrossRef]
8. Peng, J.; Xiao, J.; Yang, Y.; Dong, Y.; Zhang, J. Long-Term Experimental Study and Prediction of the Mechanical Performance on Corroded Prestressing Steel Strands Subjected to Marine Salt Spray Environment. *Constr. Build. Mater.* **2024**, *425*, 136069. [CrossRef]
9. Peng, W.; Fan, W. Experimental Study on Corrosion Development Model and Fatigue Performance of Strand Steel for Coastal Structures. *J. Mar. Sci. Eng.* **2023**, *11*, 665. [CrossRef]
10. Meng, E.; Yao, G.; Yu, Y.; Jiang, D. Analysis on Physical and Mechanical Performance and Damage Mechanism of Steel Strand under Coupling Effects of Load and Environment. *Mater. Corros.* **2018**, *69*, 1539–1547. [CrossRef]
11. Chen, Y.; Qin, W.; Wang, Q.; Tan, H. Influence of Corrosion Pit on the Tensile Mechanical Properties of a Multi-Layered Wire Rope Strand. *Constr. Build. Mater.* **2021**, *302*, 124387. [CrossRef]
12. Zhao, N.; He, Y.; Lin, L.; Liu, R.; Zhao, Q.; Zheng, W. Strength-Toughness Balance and Hydrogen Embrittlement Susceptibility of a Precipitation-Strengthened Steel Adopted Tempering Process. *Metals* **2022**, *12*, 1534. [CrossRef]
13. Chen, T.-C.; Chen, S.-T.; Tsay, L.-W.; Shiue, R.-K. Correlation between Fatigue Crack Growth Behavior and Fracture Surface Roughness on Cold-Rolled Austenitic Stainless Steels in Gaseous Hydrogen. *Metals* **2018**, *8*, 221. [CrossRef]
14. Wang, W.; Fu, H.; Zhang, H.; Yan, Y.; Li, J. Effect of Grain Orientation on Hydrogen Embrittlement Behavior of Interstitial-Free Steel. *Metals* **2022**, *12*, 981. [CrossRef]
15. Yuan, J.; Li, P.; Zhang, H.; Yin, S.; Xu, M. Electrochemical Characteristics and Corrosion Mechanisms of High-Strength Corrosion-Resistant Steel Reinforcement under Simulated Service Conditions. *Metals* **2024**, *14*, 876. [CrossRef]
16. Fideles, F.F.D.M.; Florez, M.A.C.; Rodrigues, M.V.G.; Cardoso, J.L.; Aranas, C.; Rodrigues, S.F.; Lima, M.N.D.S.; Pascoal, C.V.P.; De Moura, T.A.; Reis, G.S.; et al. Influence of the Morphology of Eutectoid Steels on Corrosion Resistance in NaCl Aqueous Medium with and without CO_2. *Metals* **2023**, *13*, 1782. [CrossRef]
17. Vignal, V.; Rault, V.; Krawiec, H.; Lukaszczyk, A.; Dufour, F. Microstructure and Corrosion Behaviour of Deformed Pearlitic and Brass-Coated Pearlitic Steels in Sodium Chloride Solution. *Electrochim. Acta* **2016**, *203*, 416–425. [CrossRef]
18. Toribio, J.; Ovejero, E. Stress Corrosion Cracking Paths in Cold Drawn Pearlitic Steels. *Procedia Struct. Integr.* **2022**, *39*, 475–478. [CrossRef]
19. Toribio, J.; Ovejero, E. Composite Microstructure of Cold-Drawn Pearlitic Steel and Its Role in Stress Corrosion Behavior. *J. Mater. Eng. Perform.* **2000**, *9*, 272–279. [CrossRef]
20. Torkkeli, J.; Saukkonen, T.; Hänninen, H. Effect of Pearlite on Stress Corrosion Cracking of Carbon Steel in Fuel-Grade Ethanol. *Corros. Rev.* **2018**, *36*, 281–293. [CrossRef]
21. Wang, L.; Li, T.; Dai, L.; Chen, W.; Huang, K. Corrosion Morphology and Mechanical Behavior of Corroded Prestressing Strands. *J. Adv. Concr. Technol.* **2020**, *18*, 545–557. [CrossRef]
22. *GB/T 21839-2019*; Test Methods for Steel for Prestressed Concrete. General Administration of Quality Supervision, Inspection and Quarantine of the People's Republic of China. Standardization Administration of China, Standards Press of China: Beijing, China, 2019.
23. Nam, W.J.; Song, H.R.; Bae, C.M. Effect of Microstructural Features on Ductility of Drawn Pearlitic Carbon Steels. *ISIJ Int.* **2005**, *45*, 1205–1210. [CrossRef]
24. Zhang, X.; Hansen, N.; Godfrey, A.; Huang, X. Dislocation-Based Plasticity and Strengthening Mechanisms in Sub-20 Nm Lamellar Structures in Pearlitic Steel Wire. *Acta Mater.* **2016**, *114*, 176–183. [CrossRef]
25. Zhang, X.; Godfrey, A.; Huang, X.; Hansen, N.; Liu, Q. Microstructure and Strengthening Mechanisms in Cold-Drawn Pearlitic Steel Wire. *Acta Mater.* **2011**, *59*, 3422–3430. [CrossRef]
26. Galvele, J.R.; Torresi, R.M.; Carranza, R.M. Passivity Breakdown, Its Relation to Pitting and Stress-Corrosion-Cracking Processes. *Corros. Sci.* **1990**, *31*, 563–571. [CrossRef]

27. Wang, Y.; Li, K.Y.; Scenini, F.; Jiao, J.; Qu, S.J.; Luo, Q.; Shen, J. The Effect of Residual Stress on the Electrochemical Corrosion Behavior of Fe-Based Amorphous Coatings in Chloride-Containing Solutions. *Surf. Coat. Technol.* **2016**, *302*, 27–38. [CrossRef]
28. Katiyar, P.K.; Misra, S.; Mondal, K. Effect of Different Cooling Rates on the Corrosion Behavior of High-Carbon Pearlitic Steel. *J. Mater. Eng. Perform.* **2018**, *27*, 1753–1762. [CrossRef]
29. Wang, Y.; Yang, Y.; Qu, J.; Cui, C. Electrochemical Dissolution of MCrAlY Coatings and Oxide Layers on Ni-Based Superalloys in 3.5% NaCl and Aqua-Regia Solutions. *Int. J. Electrochem. Sci.* **2024**, *19*, 100451. [CrossRef]
30. Zhang, Z.; Wang, L.; Huang, W.; Min, X.; Luo, G.; Wang, H.; Zhou, L.; Xie, Z.; Fang, F. Stress Corrosion Cracking Mechanisms in Bridge Cable Steels: Anodic Dissolution or Hydrogen Embrittlement. *Int. J. Hydrog. Energy* **2025**, *97*, 46–56. [CrossRef]
31. Kawamori, M.; Yuse, F. In-Situ Measurement of Hydrogen Entry and Hydrogen Embrittlement of Steel by Atmospheric Corrosion. *Corros. Sci.* **2023**, *219*, 111212. [CrossRef]